Input–Output Feedback Linearization Control of a Linear Induction Motor Taking Into Consideration Its Dynamic End-Effects and Iron Losses

Angelo Accetta , *Member, IEEE*, Maurizio Cirrincione , *Senior Member, IEEE*,
Filippo D'Ippolito , *Member, IEEE*, Marcello Pucci , *Senior Member, IEEE*,
and Antonino Sferlazza , *Member, IEEE*

Abstract—This article proposes a new input–output feedback linearization control (FLC) technique of linear induction motors (LIMs), taking into consideration both the dynamic end-effects and the iron losses. Starting from a previously conceived dynamic model, including the dynamic end-effects and the iron losses, all the theoretical framework of the FLC has been developed. The proposed FLC improves a previous version of FLC in accounting also the iron losses, which in LIMs with fixed-secondary sheet play a pivotal role more than in rotating induction motors (RIMs). The proposed FLC has been experimentally tested on a suitably developed test setup, and experimental comparisons between the proposed FLC, the classic field-oriented control and a previously developed FLC, not accounting for the iron losses, have been shown in variable flux working conditions.

Index Terms—Dynamic end-effects, input–output feedback linearization control (FLC), iron losses, linear induction motor (LIM), space-vector state model, nonlinear control.

I. INTRODUCTION

LINEAR induction motors (LIMs) have been studied for several years [2]–[5], mainly because of their ability to develop a direct linear motion without the need of any rotating-to-linear motion transformation. Today, LIMs are more and more adopted in magnetically levitation vehicles, urban people movers, X–Y-planar motion industrial platforms, launchers, actuators for industry and automotive electromagnetic rail

guns (linear tube machine), linear elevators (lift), warehouse transportation, baggage handling (conveyor belt) in the airport, linear-driven aluminum foil fabrication, and the linear-driven crane-bridge system.

The main features characterizing LIMs to their rotating counterparts [rotating induction motors (RIMs)] are the so-called end-effects. End effects in LIMs are divided into static and dynamic ones, being the latter largely more significant. The dynamic end-effects are generated by the relative motion between the primary and the secondary. Such a motion leads to a decrease of the air-gap flux density at the entrance of the motion and a decrease of it at the exit of the motion, with a consequent average demagnetization of the machine. A further effect is the increase of the overall power losses and a reduction of the propulsive force due to the rise of an end-effects braking force. Such a phenomenon increases at increasing speeds of the primary. Furthermore, because of the dynamic end-effects, most of the LIM model parameters become time-varying. For all the abovementioned reasons, the complexity and nonlinearity of the machine dynamic model increase a lot, calling for more complex and specifically devised control techniques.

As for the dynamic models, the main issues are the so-called end-effects, both static and dynamical, the latter being more important. Several dynamic models of LIMs have been developed, some of them are based on the geometrical data of the motor [6], [7], and others account for the end-effects and transversal edge effects by properly defined multiplicative coefficients [8], others account for the end-effects introducing an end-effect factor and are expressed in state form.

None of the abovementioned dynamic models, however, takes into consideration the iron losses of the LIM. Accounting for the iron losses is, in the LIM, even more significant than in the RIM, especially in the case of LIMs with fixed-secondary track. Indeed, while in the RIM, the iron losses are concentrated in the laminated stator, in the LIM they are concentrated in the unlaminated back iron of the secondary sheet, and thus, cannot be neglected.

Only recently has a dynamic model of the LIM been presented, accounting for both the dynamic end-effects and iron losses, expressed in state form [9]. The contemporary presence of the end-effects and the not negligible iron losses significantly

increases the complexity of the LIM dynamic model and, consequently, of any model-based control technique.

Recently, nonlinear control techniques have been exploited with the aim of improving the LIM drive dynamic performance as well as increasing its efficiency. In particular, Zou *et al.* [10] proposed an improved DeadBeat control (DBC) with an iterative algorithm devised to solve the voltage and current constraints problem in the traditional DBC. Xu *et al.* [11] proposed an MTPA-based finite-set model predictive control, called the finite-set model predictive direct thrust control, depending on both thrust and primary flux linkage. Xu *et al.* [12] proposed a robust speed control strategy using the sliding mode direct thrust control (SM-DTC), developed in order to achieve faster speed tracking ability with lower thrust ripple for the linear induction machine (LIM), integrated with an improved maximum thrust per ampere (MTPA) technique. Ali *et al.* [13] proposed the new supertwisting SM-DTC scheme, developed in order to improve the dynamic response, robustness ability of the linear induction machine, and overall drive performance. Elmorshedy *et al.* [14] proposed a finite-set model predictive direct flux control, depending upon the MTPA strategy, which is based on the primary flux-linkage. A novel cost function is proposed, which does not require any weighting factors in order to considerably reduce the calculation steps. Tang *et al.* [15] proposed a fuzzy weighting factor optimization method for the model predictive thrust control of LIMs, in order to identify the suitable control action.

The standard high-performance control technique of LIMs, exactly as of RIM, is the field-oriented control (FOC). The dynamic performance guaranteed by FOC, however, reduces when contemporary flux and torque/force control variations are commanded, because of the nonlinearity of the torque/force expression. Varying flux working condition typically occurs when electrical losses minimization techniques (ELMTs) are integrated into the control law. To overcome this limitation of FOC, a specific model-based nonlinear control technique can be exploited called input–output feedback linearization control (FLC) (see [16]–[18]).

Nevertheless, very few applications of nonlinear control methods to electrical drives are provided by the scientific literature. Among these few applications, a very limited number of papers deal with the input–output feedback linearization of linear induction motors (see [19]–[22]). All these papers approach the FLC of the LIM, adopting for the controller synthesis a dynamic model of the LIM, which neglects both the static and the dynamic end-effects. This corresponds to adopting the dynamic model of the equivalent RIM. The FLC presented in [23]–[25] has been specifically devised for LIMs, since it embeds in its formulation, the LIM end-effects (the dynamic ones). The FLC proposed in this article, starting from the dynamic model including the dynamic end-effects and the iron losses published in [9], proposes a new input–output FLC technique. The proposed FLC improves [23]–[25] since it permits to consider, besides the end-effect, also the iron losses. This further upgrade of the control law has been conceived because LIMs with moving primary present significant iron losses on the secondary track, which is usually not laminated. This is the theoretical motivation underlying the development of the FLC proposed in this article.
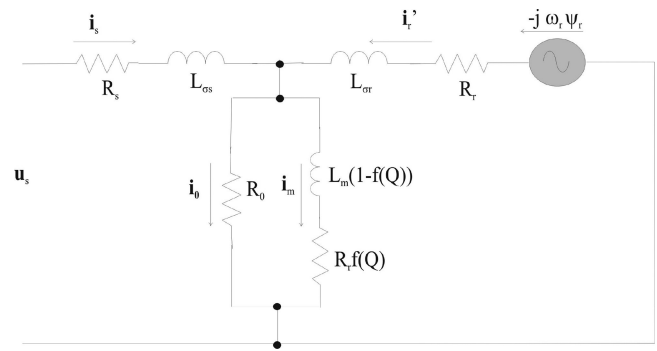

Fig. 1. Space-vector equivalent circuit of the LIM including dynamic end-effects and iron losses.

This article, starting from the dynamic model, including the dynamic end-effects and the iron losses, proposes a new input–output FLC technique. This FLC inherently accounts for both effects, and therefore, improves the FLC in [23]–[25]. The space-vector dynamic model of the LIM, which is inspired to [26] and [27], on which the proposed FLC is based, was presented in [9]. The target of the proposed FLC is to define a set of nonlinear transformations of the state variables and input of the system, permitting a decoupled control of the linear speed of the LIM and the secondary flux amplitude, in both constant flux and variable flux working conditions.

The FLC has been assessed experimentally on a suitably developed experimental rig, and experimental comparison between the proposed FLC, the classic FOC, and the FLC, not accounting for the iron losses, has been shown in variable flux working conditions.

II. STATE-SPACE-VECTOR MODEL OF THE LIM INCLUDING END-EFFECTS AND THE IRON LOSSES

The proposed FLC is based on a dynamic model of the LIM accounting for both the end-effects and the iron losses. This model was developed in [9] and, particularly, presents time-varying parameters to account for end-effects and iron losses. The equations of the model have been developed starting from the space-vector equivalent circuit of the LIM accounting for both the end-effects and iron losses, expressed in the primary reference frame, as shown in Fig. 1.

Iron losses have been modeled by a constant transversal resistance R_0. Only the fundamentals of this model are presented in the following, useful for the development of the FLC strategy, which is the main focus of this article.

A. LIM Dynamic End-Effects

The dynamic end-effects are caused by the relative motion between the short primary and the secondary track. The higher the speed of the primary track, the higher the end-effect phenomenon. This last has been taken into consideration in this article by a so-called end-effect factor Q, defined as

$$Q = \frac{\tau_m R_r}{(L_m + L_{\sigma r})v}. \tag{1}$$

It can be observed that the higher the machine speed, the higher the air-gap thickness (higher leakage inductance), and the lower the primary length, the lower the factor Q. It means that the end-effects (increase of L_{sigr}) with the machine speed and with the air-gap thickness, and it reduces with the primary length (τ_m). Correspondingly, the three-phase magnetizing inductance varies with Q in the following way:

$$\hat{L}_m = L_m\left[1 - f(Q)\right], \text{ with } \quad f(Q) = \frac{1 - e^{-Q}}{Q} \tag{2}$$

which states that the inductance virtually reduces with the end-effects accounting for an overall demagnetization of the machine.

Computation of the overall losses of the machine shows that an additional resistance appears in the transversal branch taking into consideration the eddy current joule losses. This resistance is equal to

$$\hat{R}_r = R_r f(Q). \tag{3}$$

Starting from the abovementioned definitions, the primary and secondary inductances, the global leakage factor, and the secondary time constant considering the end-effects have been defined as

$$\hat{L}_s = L_{\sigma s} + L_m\left[1 - f(Q)\right] \tag{4a}$$

$$\hat{L}_r = L_{\sigma r} + L_m\left[1 - f(Q)\right] \tag{4b}$$

$$\hat{\sigma} = 1 - \frac{L_m^2\left[1 - f(Q)\right]^2}{\left[L_{\sigma s} + L_m\left(1 - f(Q)\right)\right]\left[L_{\sigma r} + L_m\left(1 - f(Q)\right)\right]} \tag{4c}$$

$$\hat{T}_r = \frac{L_{\sigma r} + L_m\left[1 - f(Q)\right]}{R_r f(Q)}. \tag{4d}$$

B. LIM State-Space Model

If the resistance R_0 accounting for the iron losses is to be considered, then the constraint linking together with the currents in the three inductances is not valid anymore. Consequently, the electrical-state variables increase from 4 to 6. Considering that the iron losses depend on the three-phase magnetizing flux, the following set of state variables has to be chosen [9]:

$$\mathbf{x} = \begin{bmatrix} i_{sD} & i_{sQ} & \psi_{mD} & \psi_{mQ} & \psi_{rD} & \psi_{rQ} \end{bmatrix}. \tag{5}$$

Defining the space-vectors: $\mathbf{i}_s = i_{sD} + j i_{sQ}$, $\boldsymbol{\Psi}_m = \psi_{mD} + j\psi_{mQ}$, $\boldsymbol{\Psi}_r = \psi_{rD} + j\psi_{rQ}$, and $\mathbf{u}_s = u_{sD} + j u_{sQ}$, the complete space-vector state representation of the LIM, including the dynamic end-effects and the iron losses expressed in the primary reference frame, can be written in compact form as follows:

$$\frac{d}{dt}\begin{bmatrix} \mathbf{i}_s \\ \boldsymbol{\Psi}_m \\ \boldsymbol{\Psi}_r \end{bmatrix} = \begin{bmatrix} -\frac{R_0 + R_s}{L_{\sigma s}} & \frac{R_0 L_r}{\hat{L}_m L_{\sigma s} L_{\sigma r}} \\ R_0 & \frac{-R_0 L_r}{\hat{L}_m L_{\sigma r}} - \frac{\hat{R}_r}{\hat{L}_m} \\ 0 & \frac{R_r}{L_{\sigma r}} - \frac{\hat{R}_r}{\hat{L}_m} \end{bmatrix}$$

$$\begin{matrix} \frac{-R_0}{L_{\sigma s} L_{\sigma r}} \\ \frac{R_0}{L_{\sigma r}} \\ j\omega_r - \frac{R_r}{L_{\sigma r}} \end{matrix} \left.\begin{matrix} \\ \\ \end{matrix}\right] \begin{bmatrix} \mathbf{i}_s \\ \boldsymbol{\Psi}_m \\ \boldsymbol{\Psi}_r \end{bmatrix} + \begin{bmatrix} \frac{1}{L_{\sigma s}} \\ 0 \\ 0 \end{bmatrix} \mathbf{u}_s. \tag{6}$$

For the definition of symbols and variables, in particular, the time-varying parameters with ˆ, the reader can refer to [9]. Model (6) is expressed in the primary reference frame, however, in order to illustrate the proposed FLC, it is useful to transform the equations in the secondary flux reference frame, and it can be obtained by a vector rotation to an x–y-reference frame rotating with a speed equal to

$$\omega_{mr} = \omega_r + \left(\frac{R_r}{L_{\sigma r}} - \frac{\hat{R}_r}{\hat{L}_m}\right)\frac{\psi_{mq}}{|\boldsymbol{\Psi}_r|} \tag{7}$$

with x-axis aligned with the $\boldsymbol{\Psi}_r$ space-vector. The second term in (7) is the slip speed, as clearly explained in [9]. Thus, the final scalar equations are

$$\frac{di_{sx}}{dt} = -a_{11}i_{sx} + a_{12}\psi_{mx} - a_{13}\psi_{rx}$$
$$+ \left(\omega_r + a_{31}\frac{\psi_{my}}{\psi_{rx}}\right)i_{sy} + \frac{u_{sx}}{L_{\sigma s}} \tag{8a}$$

$$\frac{di_{sy}}{dt} = -\left(a_{11} + a_{31}\frac{\psi_{my}}{\psi_{rx}}\right)i_{sy} + a_{12}\psi_{my} +$$
$$- \omega_r i_{sx} + \frac{u_{sy}}{L_{\sigma s}} \tag{8b}$$

$$\frac{d\psi_{mx}}{dt} = a_{21}i_{sx} - a_{22}\psi_{mx} + \omega_r\psi_{my} + a_{31}\frac{\psi_{my}^2}{\psi_{rx}} + a_{23}\psi_{ra} \tag{8c}$$

$$\frac{d\psi_{my}}{dt} = a_{21}i_{sy} - a_{22}\psi_{my} - \omega_r\psi_{mx} + a_{31}\frac{\psi_{my}\psi_{mx}}{\psi_{rx}} \tag{8d}$$

$$\frac{d\psi_{rx}}{dt} = a_{31}\psi_{mx} - a_{32}\psi_{rx} \tag{8e}$$

where

$$a_{11} = \frac{R_s + R_0}{L_{\sigma s}}, \quad a_{12} = \frac{R_0 L_r}{\hat{L}_m L_{\sigma s} L_{\sigma r}}, \quad a_{13} = \frac{R_0}{L_{\sigma s} L_{\sigma r}}$$

$$a_{21} = R_0, \quad a_{22} = \frac{R_0 L_r}{\hat{L}_m L_{\sigma r}} + \frac{\hat{R}_r}{\hat{L}_m}, \quad a_{23} = \frac{R_0}{L_{\sigma r}}$$

$$a_{31} = \frac{R_r}{L_{\sigma r}} - \frac{\hat{R}_r}{\hat{L}_m}, \quad a_{32} = \frac{R_r}{L_{\sigma r}}.$$

In model (8), it has been considered that $\psi_{ry} = 0$, since its dynamic equation is $\frac{d\psi_{ry}}{dt} = -a_{32}\psi_{ry}$. This implies that ψ_{ry} converges to zero asymptotically independently of the operating conditions of the motor.

Finally, the mechanical equation of the motion of an LIM is

$$M\frac{dv}{dt} = F - F_L \tag{9}$$

where F is the net propulsive force generated by the LIM, F_L is the load force, and M is the overall mass of the system (motor plus payload). Differently from the RIM case, the net thrust is

the algebraic sum of the electromagnetic propulsive force F_e (similar to the torque expression of the RIM) and the braking force due to the end-effects F_{eb}. The expressions of F_e and F_{eb} are

$$F_e = \gamma M \psi_{rx} \psi_{my} \tag{10a}$$

$$F_{eb} = \eta |\mathbf{\Psi}_m|^2 \tag{10b}$$

where $\gamma = \frac{3}{2} \frac{\pi p}{\tau_p L_{\sigma r} M}$ and $\eta = \frac{3}{2} \frac{\hat{L}_r}{\hat{L}_m^2} \frac{1-e^{-Q}}{\tau_m}$. Equation (10a) provides the electromagnetic forces produced by the LIM, taking into consideration both the iron losses and the dynamic end-effects, and provides important information. Equation (10b) provides the braking force caused by the presence of the end-effects.

Indeed, the electromagnetic force of the LIM is not obtained with the vector product between the secondary flux linkage and the primary current space-vectors, but the vector product of the secondary flux linkage and the three-phase magnetizing flux space-vectors. For further detail the reader is addressed to [9].

III. FLC CONSIDERING THE LIM DYNAMIC END-EFFECTS AND THE IRON LOSSES

As for the RIM, it is well-known that FOC is able to decouple speed and flux control only in the constant flux operation. In the variable flux operation, speed and flux loops remain coupled by the torque equation. To fully decouple the speed and flux loops even in the variable flux operation, the suited approach is the input–output FLC, as given in [26] and [27].

Looking at equations shown in Section II, in particular, those describing the speed and flux dynamics, it can be easily observed that they are coupled even if the machine works at constant flux, because of the dependence of the electrical parameters on the speed. In variable flux working conditions, there is a further source of coupling between the speed and flux loops due to the propulsive force in (10a).

To overcome this problem, and obtain a fully decoupled linear model in both constant flux and variable flux conditions, a further feedback loop should be devised. With this aim, if two distinct controlled outputs are selected: 1) ψ_{rx}; and 2) v, two distinct models can be proposed: 1) the flux model; and 2) the speed model, using the feedback linearization method. The first model consists of the equations of the model described in Section II expressing the dynamics of the the flux along the x-axis ψ_{rx}. The other model consists of the equations expressing the dynamics of the mechanical speed v. Equation (11) and (12) shown at the bottom of this page.

With regards to the flux model, it is possible to compute the Lie derivatives of ψ_{rx} up to the third-order before the input u_{sx} appears in the equation. In particular, defining $x_{\psi 1} = \psi_{sx}$, $x_{\psi 2} = \dot{\psi}_{sx}$, and $x_{\psi 3} = \ddot{\psi}_{sx}$, the following equations can be written:

$$\dot{x}_{\psi 1} = x_{\psi 2}, \qquad \dot{x}_{\psi 2} = x_{\psi 3}, \qquad \dot{x}_{\psi 3} = f_\psi + b_\psi u_{sx} \tag{13}$$

where f_ψ is defined in (11), while b_ψ is defined as $b_\psi = \frac{a_{31}a_{21}}{L_{\sigma s}}$.

With regards to the speed model, it is possible to compute the Lie derivatives of v up to the third-order before that the input u_{sy} appears in the equation. In particular, defining $x_{v1} = v, x_{v2} = \dot{v}$, and $x_{v3} = \ddot{v}$, the following equations can be written:

$$\dot{x}_{v1} = x_{v2}, \qquad \dot{x}_{v2} = x_{v3}, \qquad \dot{x}_{v3} = f_v + b_v u_{sy} \tag{14}$$

where f_v is defined in (12), while b_v is defined as $b_v = \frac{\gamma a_{21} \psi_{rx}}{L_{\sigma s}}$. Note that for both models (13) and (14), in order to reduce the computational load of the controller, the derivatives of the parameter with respect to the speed are assumed zero, which is an absolutely reasonable approximation.

Models (13) and (14) show that the flux and speed models have the same structure (but with different dimensions). Moreover, choosing the control variables as follows:

$$u_{sx} = \frac{1}{b_\psi}\left(-f_\psi + \nu_x\right), \qquad u_{sy} = \frac{1}{b_v}\left(-f_v + \nu_y\right). \tag{15}$$

$$f_\psi = a_{31}a_{21}\left(-a_{11}i_{sx} + a_{12}\psi_{mx} - a_{13}\psi_{rx}\right) + \left(a_{31}a_{23} + a_{32}^2\right)\left(a_{31}\psi_{mx} - a_{32}\psi_{rx}\right) +$$

$$- a_{31}(a_{22} + a_{32}) \cdot \left(a_{21}i_{sx} - a_{22}\psi_{mx} + \omega_r\psi_{my} + a_{31}\frac{\psi_{my}^2}{\psi_{rx}} + a_{23}\psi_{rx}\right) + \frac{p\pi}{\tau_p}\left(a_{31}\gamma\psi_{my}^2\psi_{rx} - a_{31}\psi_{my}\frac{F_L}{M}\right)$$

$$+ a_{31}\omega_r\left(a_{21}i_{sy} - a_{22}\psi_{my} - \omega_r\psi_{mx} - a_{31}\frac{\psi_{mx}\psi_{my}}{\psi_{rx}}\right) + -a_{31}^2\frac{\psi_{my}^2}{\psi_{rx}^2}\left(a_{31}\psi_{mx} - a_{32}\psi_{ra}\right)$$

$$+ 2a_{31}^2\frac{\psi_{my}}{\psi_{rx}}\left(a_{21}i_{sy} - a_{22}\psi_{my} - \omega_r\psi_{mx} - a_{31}\frac{\psi_{mx}\psi_{my}}{\psi_{rx}}\right) \tag{11}$$

$$f_v = \gamma\psi_{rx}a_{21}\left(-a_{11}i_{sy} + a_{12}\psi_{my} - \omega_r i_{sy} - a_{31}\frac{\psi_{my}i_{sy}}{\psi_{rx}}\right) + \gamma\left(a_{31}\psi_{mx} - a_{32}\psi_{rx}\right)\left(a_{21}i_{sy} - (a_{32} + a_{22})\psi_{my} - \omega_r\psi_{mx}\right) +$$

$$- \gamma\psi_{rx}(a_{32} + a_{22})\left[a_{21}i_{sy} - a_{22}\psi_{my} + \left(\omega_r + a_{31}\frac{\psi_{my}}{\psi_{rx}}\right)\psi_{mx}\right] - \gamma\psi_{rx}\left(\gamma\psi_{rx}\psi_{my} - \frac{F_L}{M}\right)\psi_{mx} +$$

$$- \gamma\psi_{rx}\omega_r\left(a_{21}i_{sx} - a_{22}\psi_{mx} + \omega_r\psi_{my} + a_{31}\frac{\psi_{my}^2}{\psi_{rx}} + a_{23}\psi_{rx}\right) \tag{12}$$
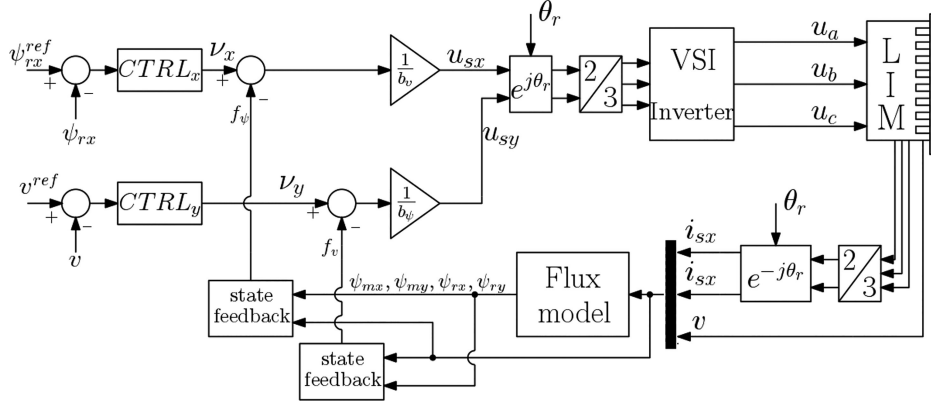
Fig. 2.   Block diagram of the proposed control scheme of the LIM drive.

Models (13) and (14) become two chains of integrators as follows:

$$\dot{x}_{\psi 1} = x_{\psi 2}, \qquad \dot{x}_{\psi 2} = x_{\psi 3}, \qquad \dot{x}_{\psi 3} = \nu_x \qquad (16)$$

$$\dot{x}_{v 1} = x_{v 2}, \qquad \dot{x}_{v 2} = x_{v 3}, \qquad \dot{x}_{v 3} = \nu_y. \qquad (17)$$

Therefore, ν_x and ν_y can be designed by using classical tools for linear systems to satisfy the design requirements for linear models (16) and (17).

In summary, to achieve the input–output feedback linearizing control of LIM, considering both the end-effects and the iron losses, the inputs ν_x and ν_y have to be selected through a first-state feedback to fix the flux and speed dynamics. Then, through a second-state feedback, the voltage sources u_{sx} and u_{sy} are obtained starting from ν_x and ν_y by means of (15). Note that the only condition to ensure the existence of this feedback is that the flux $|\psi_{rx}|$ is different from zero. Finally, it is useful to note that the linearization terms in (11) and (12) have never been shown in literature, and they have been obtained specifically in this article to account for both end-effects and iron losses.

The block diagram of the feedback control scheme of the LIM drive is shown in Fig. 2.

A. Design of Flux and Speed Controllers

In order to make ψ_r and v tracks, the references ψ_{ref} and v_{ref} and the input signals ν_x and ν_y are designed as

$$\nu_x = -k_{\psi 1}\left(x_{\psi 1} - \psi_{\mathrm{ref}}\right) - k_{\psi 2}\left(x_{\psi 2} - \frac{d\psi_{\mathrm{ref}}}{dt}\right) +$$
$$- k_{\psi 3}\left(x_{\psi 3} - \frac{d^2\psi_{\mathrm{ref}}}{dt^2}\right) + \frac{d^3\psi_{\mathrm{ref}}}{dt^3} \qquad (18)$$

$$\nu_y = -k_{v 1}\left(x_{v 1} - v_{\mathrm{ref}}\right) - k_{v 2}\left(x_{v 2} - \frac{dv_{\mathrm{ref}}}{dt}\right) +$$
$$- k_{v 3}\left(x_{v 3} - \frac{d^2 v_{\mathrm{ref}}}{dt^2}\right) + \frac{d^3 v_{\mathrm{ref}}}{dt^3} \qquad (19)$$

where $k_{\psi 1}$, $k_{\psi 2}$, $k_{\psi 3}$, $k_{v 1}$, and $k_{v 2}$ are the positive constant design parameters. These are determined in order to impose an exponentially stable dynamic of the decoupled, linear, time-invariant, and systems constituted by the flux and speed errors

$e_{\psi_r} = \psi_r - \psi_{\mathrm{ref}}$ and $e_v = v - v_{\mathrm{ref}}$

$$\frac{d^3 e_{\psi_r}}{dt^3} = -k_{\psi 1} e_{\psi_r} - k_{\psi 2}\frac{de_{\psi_r}}{dt} - k_{\psi 3}\frac{d^2 e_{\psi_r}}{dt^2} \qquad (20)$$

$$\frac{d^2 e_v}{dt^2} = -k_{v 1} e_v - k_{v 2}\frac{de_v}{dt} - k_{v 3}\frac{d^2 e_v}{dt^2}. \qquad (21)$$

In particular, it is possible to assign both flux and speed dynamics by choosing suitably the zeros of the following characteristic polynomials:

$$\Delta_\psi(\lambda) = k_{\psi 1} + k_{\psi 2}\lambda + k_{\psi 3}\lambda^2 + \lambda^3 \qquad (22)$$

$$\Delta_v(\lambda) = k_{v 1} + k_{v 2}\lambda + k_{v 3}\lambda^2 + \lambda^3. \qquad (23)$$

In this case, the parameters have been determined assuming that the desired zeros are $\lambda_1 = -\zeta\omega_n + j\omega_n\sqrt{1 - \zeta^2}$, $\lambda_2 = -\zeta\omega_n - j\omega_n\sqrt{1 - \zeta^2}$, and $\lambda_3 = \sigma$, where ω_n and ζ are the natural frequency and the damping factor, respectively, while σ is a negative real number. This choice ensures an exponentially stable error dynamics.

To compare the FLC with the FOC, the parameters ω_n, ξ, and σ (for both speed and induced part flux loop) and the parameters of the PI in the FOC, have to be chosen such that the two closed-loop systems present the same closed-loop dynamics. In particular, both for FOC and FLC, the Bode diagrams of the transfer functions of the closed-loop systems, plotted in Figs. 3 and 4, are obtained.

From these figures, it can be easily observed that the two systems: 1) LIM controlled with FLC; and 2) LIM controlled with FOC, respectively, have the same bandwidths equal to 456 rad/s for the secondary flux loop and 37 rad/s for the speed loop, respectively. Moreover, in correspondence of the cutoff frequency, the systems have the same phase equal to $-140°$ for the induced part flux loop and $-53°$ for the speed loop, respectively. However, to obtain the transfer functions in the FOC case, the assumptions of constant parameters and constant flux amplitude have to be made. In particular, the parameters obtained at rated speed and rated flux are considered.

IV. TEST SET-UP

A test setup has been suitably built to experimentally verify the goodness of the proposed input–output feedback linearization
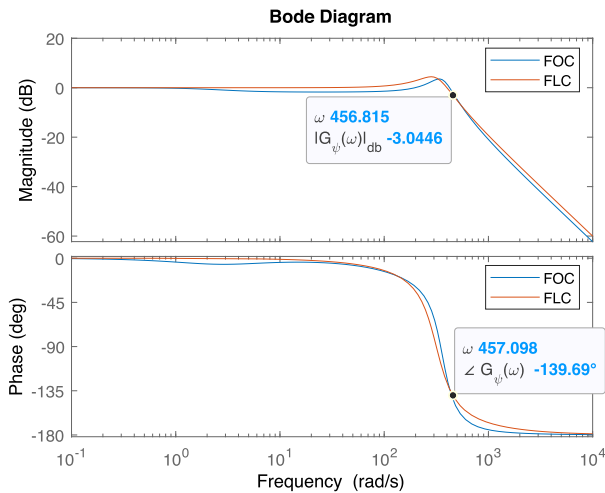
Fig. 3. Bode diagram of the closed-loop transfer function of the indiced part flux.
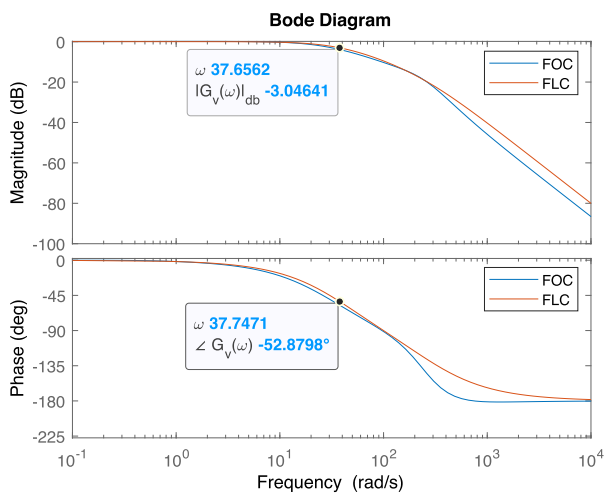

Fig. 4. Bode diagram of the closed-loop transfer function of the speed.

TABLE I
PARAMETERS OF THE LIM MODEL

SYMBOLS	VALUES
Rated power (W)	425
Rated voltage (V)	380
Rated frequency (Hz)	60
Pole-pairs	3
Rated speed (m/s)	6.85
Mass (kg)	20
Inductor resistance R_s (Ω)	11
Inductor inductance L_s (mH)	634
Induced part resistance R_r (Ω)	32.6
Induced part inductance L_r (mH)	758
3-phase magnetizing inductance L_m (mH)	517

technique considering both the end-effects and the iron losses. The LIM under test is a Baldor LMAC1607C23D99, whose rated data and electrical parameters are given in Table I. The LIM has been equipped with a linear encoder Numerik Jena LIA series, and it presents a secondary track of length 1.6 m. Fig. 5 shows a photograph of the test setup. The employed test setup consists of the following.
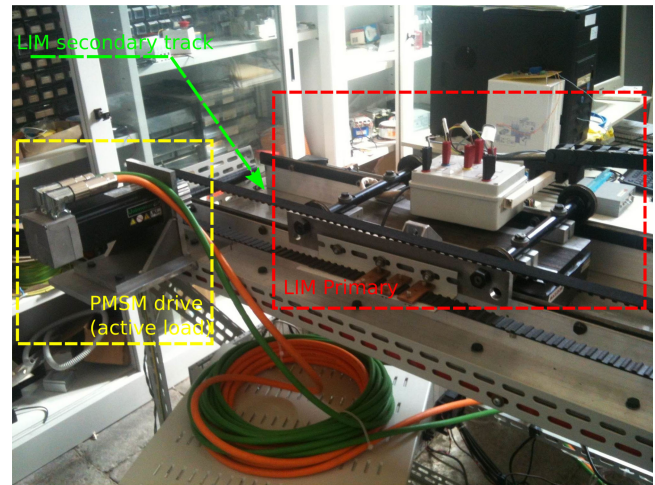
1) A three-phase linear induction motor.

Fig. 5. Photograph of the LIM experimental setup.

2) A frequency converter composed of a three-phase diode rectifier and a 7.5 kVA three-phase VSI.
3) A dSPACE card (DS1103) with a PowerPC 604e running at 400 MHz and a floating-point DSP TMS320F240.

The test setup is also equipped with a permanent magnet synchronous motor (PMSM) Emerson Unimotor HD 067UDB305BACRA, which is mechanically coupled to the LIM by a pulley-strap system to behave as an active load.

V. EXPERIMENTAL RESULTS

The proposed input–output FLC has been experimentally tested on the abovementioned test setup. Because of the limited length of the secondary track (1.6 m), the experimental test has been performed at low-speed 0.7 m/s (about 10% of the rated speed). Two experimental tests have been performed.

The drive has been given a set of speed steps, including a start-up, a speed reversal, and fast braking, of the type $0 \rightarrow 0.7 \rightarrow -0.7 \rightarrow 0$ m/s. The test has been performed twice, first, at no-load, and second, applying and releasing a step load force of 30 N during the steady-state operations of the drive at ± 0.7 m/s. As for the application of the load force, the torque-controlled PMSM drive cited in Section IV has been adopted. To emphasize the advantages arising from the adoption of the proposed FLC considering both the dynamic end-effects and the iron losses, the drive control has been integrated with the ELMT suitably developed for LIMs [28], permitting a variable flux operation of the drive. Finally, the abovementioned tests have been performed with both the proposed FLC and the classic FOC, in particular, a secondary flux-oriented control, to emphasize the improvements achievable with the adoption of the proposed FLC in a variable flux operation.

Fig. 6 shows the reference and measured speed during the test at no load. Fig. 7 shows the corresponding waveforms of the i_{sx} and i_{sy} stator current components, and finally, Fig. 8 shows the reference and estimated values of the secondary flux amplitude.

All these figures show that the proposed FLC permits a very high dynamic performance, with the propulsive component of the stator current (i_{sy}) presenting a step-wise waveform, occurring at each speed transient of the LIM drive. Even the
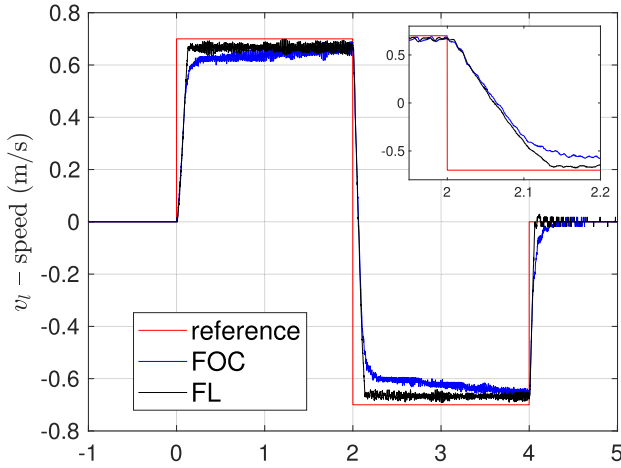
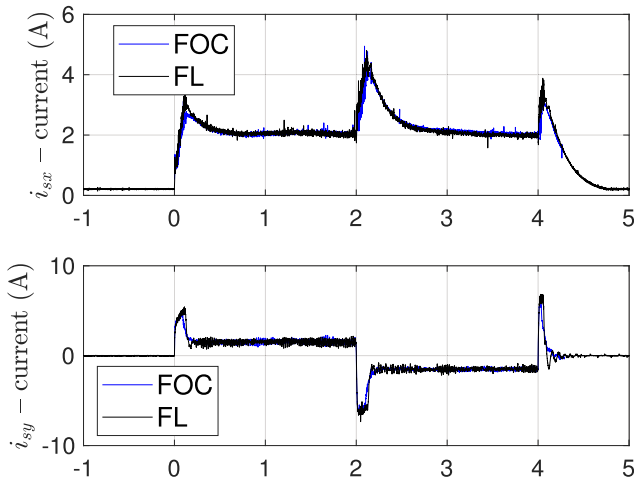Fig. 6. Reference and measured speed during a speed reversal from 0.7 to −0.7 m/s.

Fig. 7. Direct and quadrature primary current components i_{sx} and i_{sy} during a speed reversal from 0.7 to −0.7 m/s.
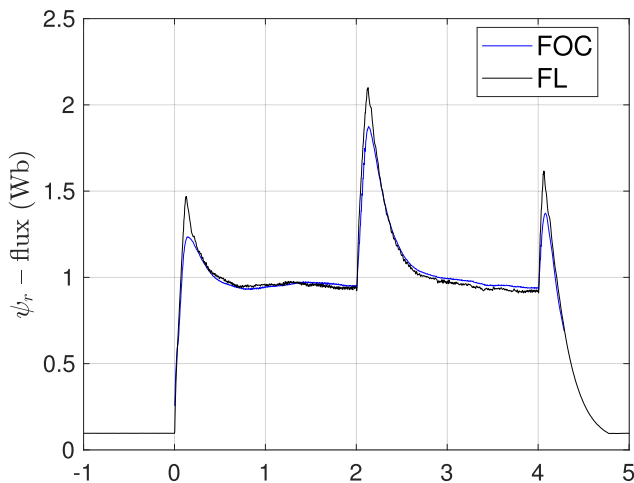

Fig. 8. Secondary $|\Psi_r|$ and three-phase magnetizing $|\Psi_m|$ flux amplitudes during a speed reversal from 0.7 to −0.7 m/s.

TABLE II
PERFORMANCES INDEXES

	IAE= $\int_0^t \left| v_l^{ref} - v_l \right| dt$		IAE= $\int_0^t \left| \psi_r^{ref} - \psi_r \right| dt$	
	FLC	FOC	FLC	FOC
Test 1	0.127	0.167	$6.6 \cdot 10^{-3}$	$7.1 \cdot 10^{-3}$
Test 2	0.129	0.184	$2.1 \cdot 10^{-3}$	$2.3 \cdot 10^{-3}$
	NEW FLC	FLC IN [23]	NEW FLC	FLC IN [23]
Test 3	1.48	3.81	0.19	0.31
Test 4	15.3	20.5	$1.49 \cdot 10^{-3}$	$68.9 \cdot 10^{-3}$

magnetizing component of the stator current (i_{sx}) presents a waveform analogous to that of the propulsive one, due to the presence of the ELMT. Both current components are controlled with very fast dynamics even in variable flux operation, thanks to the adoption of the proposed FLC. It can be noted that FOC presents a comparable dynamic of the stator current components, even if it does not straightforwardly imply comparable dynamics of the speed loop, as it is observable from the speed waveform and theoretically expected. The secondary flux amplitude waveform shows a flux increase at each commanded speed transient, as expected because of the ELMT. It further shows that the steady-state value of the flux at ±0.5 m/s is much higher than that at zero speed, witnessing that even at no load, the LIM drive is loaded with a significant friction force. Finally, the speed waveform shows a very quick response of the LIM drive, getting the steady-state speed in less than 0.3 s and accomplishing the speed reversal in about 0.5 s.

The comparison with the FOC clearly shows that dynamic performance achievable with the proposed FLC is much higher, with a much lower settling time. In particular, the zoom of the reversal clearly shows that, while at the very first instants FOC presents comparable response, in the second part of the transient FLC significantly outperforms it. These considerations are confirmed by the analysis of the integral absolute error (IAE) of the flux and speed loops provided in Table II. It must be noted that the experimental setup presents a significant friction load; if such a friction load were lower (closer to a real no-load test), the expected improvements obtained with the proposed FLC would be higher.

Figs. 9, 10, and 11 show the analogous waveforms obtained during the test in which the load force is applied. Differently from the no-load test, when the load step force is applied, a sudden increase of i_{sy} is visible, which corresponds to an analogous increase of i_{sx} and flux, because of the ELMT. The speed waveform confirms better dynamic performance obtained with the proposed FLC to FOC and a better load rejection capability, as expected.

To highlight the advantages, in terms of dynamic performance, due to the integration of the iron losses formulation in the FLC design, a high-speed test has been performed. In particular, at $t = 1$ s, contemporary reference steps of the speed equal to 5 m/s (close to the rated speed) and the secondary flux equal to 1 Wb (rated flux) have been given to the drive. At $t = 5$ s, a load step force of 50 N has been applied to the drive. Because of the limited length of the secondary track, such a test cannot be performed experimentally, thus, it has been done in numerical simulation. As LIM under test, the
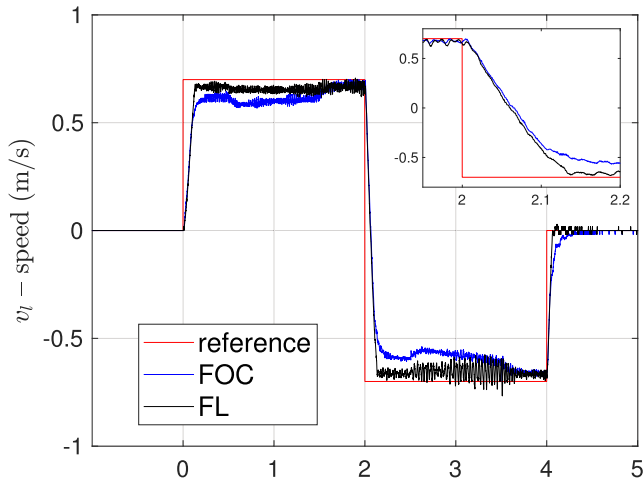
Fig. 9.　Reference and measured speed during a load step insertion and release of 30 N at a constant speed of 0.7 m/s.
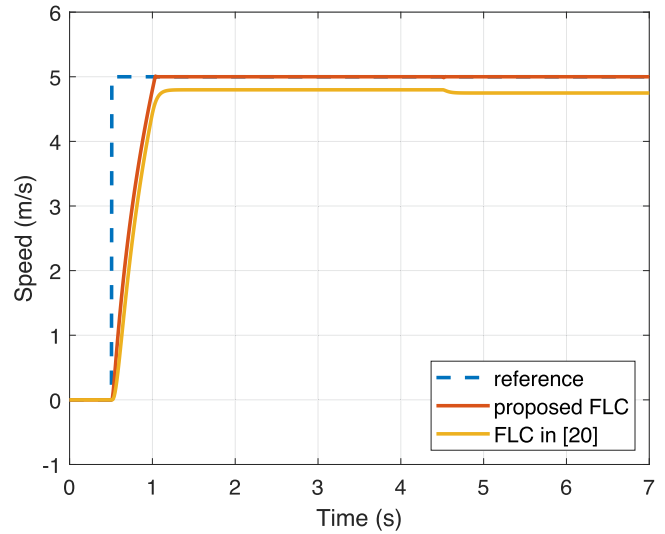

Fig. 10.　Direct and quadrature primary current components i_{sx} and i_{sy} during a load step insertion and release of 30 N at a constant speed of 0.7 m/s.

Fig. 11.　Secondary $|\mathbf{\Psi}_r|$ and three-phase magnetizing $|\mathbf{\Psi}_m|$ flux amplitudes during a load step insertion and and release of 30 N at a constant speed of 0.7 m/s.

Fig. 12.　Reference and measured speed and electromagnetic thrust during a high-speed field weakening test.
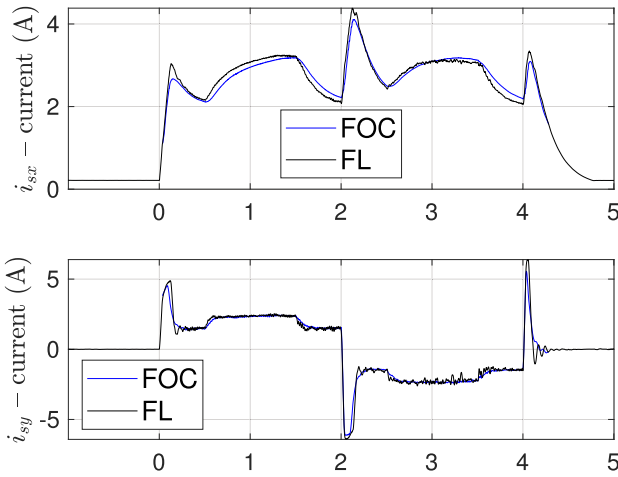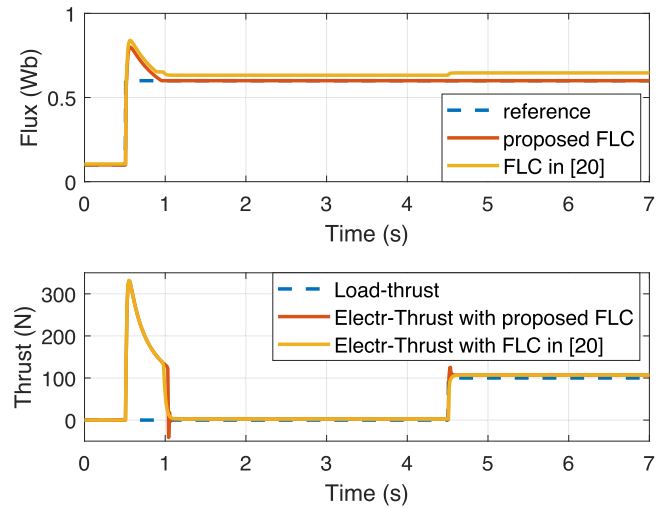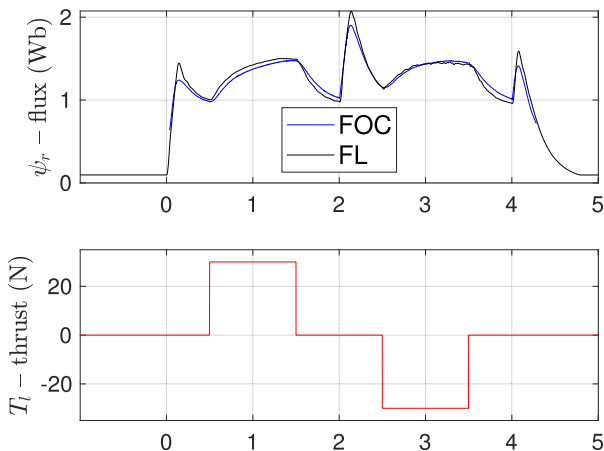

Fig. 13.　Secondary $|\mathbf{\Psi_r}|$ flux amplitude and electromagnetic thrust during a high-speed field weakening test.

dynamic model of the LIM accounting for both the iron losses and end-effects has been adopted [9], whose parameters had been identified with the procedure in [29]. The proposed FLC has been compared with the previously developed FLCs [23], [24] considering only the end-effects, to emphasize the advantages arising from embedding, in the control design, the iron losses. Fig. 14 shows the reference and measured speed with both controllers, while Fig. 15 shows the reference and estimated secondary flux amplitude, as well as the electromagnetic thrust and the load force, with both controllers. In these figures, the red line refers to the proposed FLC considering both end-effects and iron losses, while the yellow line refers to the previously developed FLC [23].

It can be observed that, because of the structure of the linear speed and flux controllers not presenting poles in the origin, the steady-state errors of both variables are non-null; the higher the proportional gains, the lower the steady-state errors, as
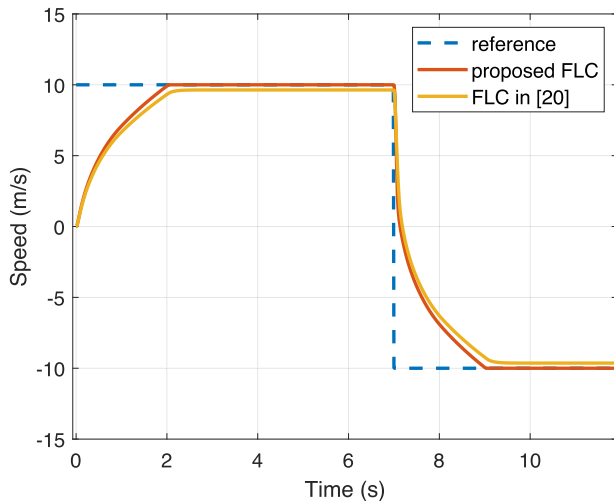
Fig. 14. Reference and measured speed during a nominal-speed test at full load.
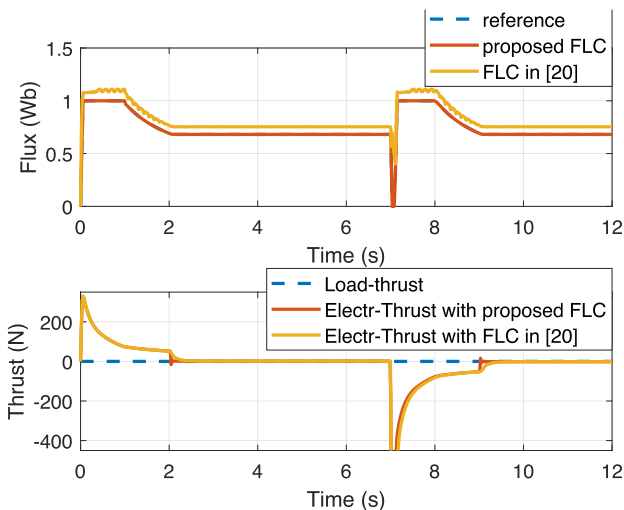

Fig. 15. Secondary $|\Psi_r|$ flux amplitude during a nominal-speed test at full load.

expected. Furthermore, the more accurate is the dynamic model underlying the FLC, the lower is the tracking errors of the controlled variables. For the abovementioned reasons, while the proposed FLC permits a steady-state tracking error of both variables, which is close to zero, thanks to the correctness of the model underlying the nonlinear transformations of the state and inputs, the FLC in [23] presents significant non-null steady-state tracking errors (in particular on the secondary flux amplitude), due to the unmodeled dynamics generated by the presence of significant iron losses. When the load force is applied, for the abovementioned reasons, the thrust increases to cope with the load force with both FLCs, but the speed tracking error increases more with the FLC in [23]. Finally, the dynamic performance achieved in the control of both the flux and the speed is sensibly higher with the proposed FLC than with [23].

The last test is a very high-speed test. Even in this case, the proposed FLC has been compared with the FLC presented in [23]. The LIM drive has been given contemporary steps of

secondary flux equal to 1 Wb and speed equal to 10 m/s (in the field weakening region) at no load. At $t = 6$ s, a speed reversal from 10 to -10 m/s has been commanded. Fig. 12 shows the reference and the measured speed, respectively, while Fig. 13 shows the reference and estimated secondary flux as well as the electromagnetic thrust and the load force. Results are coherent with the previous high-speed test. As the speed of the LIM increases, the proposed FLC overcomes the FLC in [23] in terms of dynamic performance. This is observable during the speed reversal where contemporary speed and flux variations occur. As explained above, moreover, the proposed FLC permits a lower tracking error of both the speed and the flux at steady-state, thanks to the better modeling of the LIM behavior. The IAE control indexes in Table II confirm such considerations.

VI. CONCLUSION

This article proposed a new input–output FLC technique of LIMs taking into consideration both the dynamic end-effects and the iron losses. Starting from a previously conceived dynamic model, including the dynamic end-effects and the iron losses, all the theoretical framework of the FLC was developed. The proposed FLC improves a previously proposed version of FLC since it considers also the iron losses, which play a more important role in the LIM than in the RIM. The proposed FLC was experimentally tested on a suitably developed test setup. Moreover, the experimental comparison between the proposed FLC and the FOC confirmed the better dynamic performance obtained with the proposed control technique.

REFERENCES

[1] A. Accetta, M. Cirrincione, F. D'Ippolito, M. Pucci, and A. Sferlazza, "Input-output feedback linearization control of a linear induction motor taking into consideration its dynamic end-effects and iron losses," in *Proc. IEEE Energy Convers. Congr. Expo.*, 2020, pp. 2419–2424.
[2] E. R. Laithwaite, "Linear electric machines- A personal view," *Proc. IEEE*, vol. 63, no. 2, pp. 250–290, Feb. 1975.
[3] S. Yamamura, *Theory of Linear Induction Motors*. New York, NY, USA: Halsted Press, 1979.
[4] S. A. Nasar and I. Boldea, *Linear Electric Motors: Theory, Design, and Practical Application*. Englewood Cliffs, NJ, USA: Prentice-Hall, 1987.
[5] W. Xu, M. R. Islam, and M. Pucci, *Advanced Linear Machines and Drive Systems*. Berlin, Germany: Springer, 2019.
[6] G. Gentile, N. Rotondale, and M. Scarano, "Analysis of the transient behaviour of the linear motor," *L'Energia Elettrica*, no. 5, pp. 205–212, 1987.
[7] G. Gentile, N. Rotondale, and M. Scarano, "The linear induction motor in transient operation," *L'Energia Elettrica*, no. 7-8, 1988.
[8] W. Xu *et al.*, "Equivalent circuits for single-sided linear induction motors," *IEEE Trans. Ind. Appl.*, vol. 46, no. 6, pp. 2410–2423, Nov./Dec. 2010.
[9] A. Accetta, M. Cirrincione, M. Pucci, and A. Sferlazza, "State space-vector model of linear induction motors including end-effects and iron losses part I: Theoretical analysis," *IEEE Trans. Ind. Appl.*, vol. 56, no. 1, pp. 235–244, Nov. 2019.
[10] J. Zou, W. Xu, and C. Ye, "Improved deadbeat control strategy for linear induction machine," *IEEE Trans. Magn.*, vol. 53, no. 6, pp. 1–4, Jun. 2017.
[11] W. Xu, M. F. Elmorshedy, Y. Liu, J. Rodriguez, and C. Garcia, "Maximum thrust per ampere of linear induction machine based on finite-set model predictive direct thrust control," *IEEE Trans. Power Electron.*, vol. 35, no. 7, pp. 7366–7378, Jul. 2019.
[12] W. Xu, M. M. Ali, M. F. Elmorshedy, S. M. Allam, and C. Mu, "One improved sliding mode DTC for linear induction machines based on linear metro," *IEEE Trans. Power Electron.*, vol. 36, no. 4, pp. 4560–4571, Apr. 2020.

[13] M. M. Ali, W. Xu, A. K. Junejo, M. F. Elmorshedy, and Y. Tang, "One new super-twisting sliding mode direct thrust control for linear induction machine based on linear metro," *IEEE Trans. Power Electron.*, vol. 37, no. 1, pp. 795–805, Jan. 2021.

[14] M. F. Elmorshedy, W. Xu, S. M. Allam, J. Rodriguez, and C. Garcia, "MTPA-based finite-set model predictive control without weighting factors for linear induction machine," *IEEE Trans. Ind. Electron.*, vol. 68, no. 3, pp. 2034–2047, Mar. 2020.

[15] L. Tang, W. Xu, X. Wang, D. Dong, X. Xiao, and Y. Zhang, "Weighting factors optimization of model predictive control based on fuzzy thrust constraints for linear induction machine," *IEEE Trans. Appl. Supercond.*, vol. 31, no. 8, pp. 1–5, Nov. 2021.

[16] H. K. Khalil, *Nonlinear Systems*. Englewood Cliffs, NJ, USA: Prentice-Hall, 2002.

[17] J.-J. E. Slotine *et al.*, *Applied Nonlinear Control*, vol. 199. Englewood Cliffs, NJ, USA: Prentice-Hall, 1991.

[18] A. Isidori, *Nonlinear Control Systems*, vol. 3. Berlin, Germany: Springer, 1995.

[19] F.-J. Lin and R.-J. Wai, "Hybrid control using recurrent fuzzy neural network for linear induction motor servo drive," *IEEE Trans. Fuzzy Syst.*, vol. 9, no. 1, pp. 102–115, Feb. 2001.

[20] F.-J. Lin and R.-J. Wai, "Robust control using neural network uncertainty observer for linear induction motor servo drive," *IEEE Trans. Power Electron.* vol. 17, no. 2, pp. 241–254, Mar. 2002.

[21] C.-I. Huang and L.-C. Fu, "Passivity based control of the double inverted pendulum driven by a linear induction motor," in *Proc. IEEE Conf. Control Appl.*, 2003, pp. 797–802.

[22] R.-J. Wai and C.-C. Chu, "Robust petri fuzzy-neural-network control for linear induction motor drive," *IEEE Trans. Ind. Electron.*, vol. 54, no. 1, pp. 177–189, Feb. 2007.

[23] F. Alonge, M. Cirrincione, M. Pucci, and A. Sferlazza, "Input-output feedback linearizing control of linear induction motor taking into consideration the end-effects. Part I: Theoretical analysis," *Control Eng. Pract.*, vol. 36, pp. 133–141, 2015.

[24] F. Alonge, M. Cirrincione, M. Pucci, and A. Sferlazza, "Input-output feedback linearization control with on-line MRAS-based inductor resistance estimation of linear induction motors including the dynamic end effects," *IEEE Trans. Ind. Appl.*, vol. 52, no. 1, pp. 254–266, Jan./Feb. 2016.

[25] F. Alonge, M. Cirrincione, F. D'ippolito, M. Pucci, and A. Sferlazza, "Adaptive feedback linearizing control of linear induction motor considering the end-effects," *Control Eng. Pract.*, vol. 55, pp. 116–126, 2016.

[26] R. Marino, P. Tomei, and C. M. Verrelli, *Induction Motor Control Design*. Berlin, Germany: Springer, 2010.

[27] R. Marino, S. Peresada, and P. Valigi, "Adaptive input-output linearizing control of induction motors," *IEEE Trans. Autom. Control*, vol. 38, no. 2, pp. 208–221, Feb. 1993.

[28] A. Accetta, M. C. Di Piazza, M. Luna, and M. Pucci, "Electrical losses minimization of linear induction motors considering the dynamic end-effects," *IEEE Trans. Ind. Appl.*, vol. 55, no. 2, pp. 1561–1573, Mar. 2019.

[29] A. Accetta, M. Cirrincione, M. Pucci, and A. Sferlazza, "State-space vector model of linear induction motors including end-effects and iron losses part II: Model identification and results," *IEEE Trans. Ind. Appl.*, vol. 56, no. 1, pp. 245–255, Nov. 2019.

Angelo Accetta (Member, IEEE) received the master's degree in electrical engineering in 2008 from the University of Palermo, Palermo, Italy, where he received the Ph.D. degree in electrical engineering, in collaboration with the Institute for Studies on Intelligent Systems for Automation (ISSIA) - National Research Council (CNR), Palermo, Italy, in 2011.

From 2013 to 2018, he was a Junior Researcher with the Section of Palermo, ISSIA-CNR, working to new energy management strategies for distributed generation systems and to the implementation of new sensorless control strategies for permanent magnet synchronous electric motors (PMSM) and for induction motors both rotating (RIM) and linear (LIM). He is currently a Junior Researcher with the Institute of Marine Engineering (INM), CNR. His research interests include sensorless control systems for electric drives with induction, i.e., rotating and linear, motors, with particular attention to their applications for electric generation systems and electric propulsion.
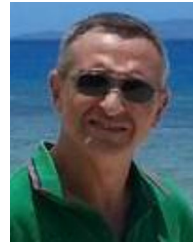
Maurizio Cirrincione (Senior Member, IEEE) received the Laurea degree in electrical engineering from the Polytechnic University of Turin, Turin, Italy, in 1991 and the Ph.D. degree in electrical engineering from the University of Palermo, Palermo, Italy, in 1996.

From 1996 to 2005, he was a Researcher with the Section of Palermo, Institute for Studies on Intelligent Systems for Automation (ISSIA) - National Research Council (CNR), Palermo, Italy. In 2005, he joined the University of Technology of Belfort-Montbeliard, Belfort, France, as a Full Professor. He is currently the Head of the "School of Engineering and Physics," University of the South Pacific, Suva, Fiji. His current research interests include neural networks for modeling and control, system identification, intelligent control, power electronics, renewable energy systems, and electrical machines and drives. Dr. Cirrincione was awarded the 1997 "E.R.Caianiello" prize for the best Italian Ph.D. thesis on neural networks.

Filippo D'Ippolito was born in Palermo, Italy, in 1966. He received the Laurea degree in electronic engineering and the Research Doctorate degree in systems and control engineering from the University of Palermo Palermo, Italy, in 1991and 1996, respectively.

He is currently a Research Associate with the Department of Electrical and Information Engineering and Mathematical Model, University of Palermo. His research interests include control of electrical drives, adaptive and visual/force control of robot manipulators, and control of electrical power converters.

Dr. Di'Ippolito received the 2000 Kelvin Premium from the Istitution of Electrical Engineers (IEE), for the paper: Parameter identification of induction motor model using genetic algorithms.

Marcello Pucci (Senior Member, IEEE) received the Laurea and Ph.D. degrees in electrical engineering from the University of Palermo, Palermo, Italy, in 1997 and 2002, respectively.

In 2000, he was a Host Student with the Institute of Automatic Control, Technical University of Braunschweig, Braunschweig, Germany, working in the field of control of ac machines, with a grant from the German Academic Exchange Service. From 2001 to 2018, he was with the Institute of Intelligent Systems for Automation, Section of Palermo, National Research Council (CNR), Palermo, Italy. He is currently a Senior Researcher with the Institute of Marine Engineering (INM), CNR. His current research interests include electrical machines; control, diagnosis, and identification techniques of electrical drives, and intelligent control and power converters.

Dr. Pucci serves as an Associate Editor for the IEEE TRANSACTIONS ON INDUSTRIAL ELECTRONICS and IEEE TRANSACTIONS ON INDUSTRY APPLICATIONS. He is a member of the Editorial Board of the *Journal of Electrical Systems*.

Antonino Sferlazza (Member, IEEE) was born in Palermo, Italy, in 1987. He received the masters degree in automation engineering and the Ph.D. degree in mathematics and automation from the University of Palermo, Palermo, Italy, in 2011 and 2015, respectively.

In 2013, he was a visiting Ph.D. student with the University of California at Santa Barbara, Santa Barbara, CA, USA, in the field of modeling and analysis of stochastic hybrid systems. From 2016 to 2017, he was with the University of Palermo as Junior Researcher. From 2017 to 2018, he was a Researcher with LAAS CNRS, Toulouse, France, working in the field of control of power converter. He is currently a Researcher in systems and control engineering with the University of Palermo. His research interests include the development of feedback control algorithms for nonlinear dynamical systems, optimization techniques, estimation of stochastic dynamical systems, and applications of control of electrical drives, power converters, and mechanical systems.